Optimizing the Thermoelectric Performance of InGaZnO Thin Films Depending on Crystallinity via Hydrogen Incorporation

Jenichi Clairvaux Felizco*, Mutsunori Uenuma*, Yasuaki Ishikawa and Yukiharu Uraoka

Graduate School of Science and Technology, Nara Institute of Science and Technology, 8916-5 Takayama, Ikoma, Nara 630-0192 Japan.

E-mail: uenuma@ms.naist.jp, jenichi.felizco.jz1@ms.naist.jp

The thermoelectric power factor of amorphous (a-IGZO), c-axis aligned crystalline (c-IGZO) and (cc-IGZO) crystal-embedded c-axis aligned crystalline InGaZnO were optimized by performing hydrogen incorporation via post-annealing. Highest power factor was achieved for a-IGZO when annealing with pure N_2 was used, while adding 4% H_2 in the N_2 atmosphere significantly enhanced those of c-IGZO and cc-IGZO. However, the cc-IGZO samples displayed weaker properties compared to both a-IGZO and c-IGZO regardless of the annealing conditions. The presence of H_2 was effective in passivating oxygen-related defects for both the c-IGZO and cc-IGZO samples, which translated to better electron transport while maintaining a respectable Seebeck coefficient. On the other hand, the formation of a high amount of oxygen vacancies from annealing with pure N_2 was likely responsible not only for the good electrical conductivity of a-IGZO, but also for the relatively good Seebeck coefficients. Establishing the post-annealing conditions to maximize the thermoelectric properties depending on crystallinity paves the way for future commercial transparent IGZO thermoelectric devices.

1. Introduction

InGaZnO (IGZO) has recently been gaining attention as a next generation material for transparent, flexible device electronics owing to its superior carrier mobility and excellent optical transparency [1–5]. A great deal of effort has been dedicated to engineer its structure to improve its electrical properties, whether in amorphous, crystalline or nanostructured form [6–8]. It has been a well-established candidate for thin film transistors as well as memory devices [9–12]. Gearing towards the realization of transparent systems-on-panel, other applications for IGZO are currently being explored. Some of these include energy devices such as solar cells and thermoelectric devices [13–16].

A thermoelectric material is one that can directly convert heat into electrical energy without the need for any moving parts. The measure for good thermoelectricity lies on achieving high thermoelectric figure of merit (ZT) values, as defined by the following equation: $ZT = S^2\sigma/\kappa$, where S is the Seebeck coefficient, σ is the electrical conductivity, and κ is the thermal conductivity. The numerator value $S^2\sigma$ is also known as the thermoelectric power factor (PF), and is known to be difficult to maximize due to the conflicting relationships of S and σ with carrier concentration. There are previous reports on the viability of IGZO as a thermoelectric material due to the following reasons. First, its σ is easily tunable by varying the carrier concentration [14]. Our group has previously reported on the PF and thermal conductivity of amorphous InGaZnO, as well as its applicability in flexible TEGs, but the study has been limited to optimizing the oxygen vacancies (Vo) by varying the oxygen partial pressure during deposition [14–15]. Second, its natural superlattice structure could reduce κ due to enhanced interface phonon scattering [16].

In a study by Cui et. al, the cross-plane κ of amorphous, semi-crystalline and crystalline IGZO were discussed. In their report, both amorphous and crystalline IGZO were regarded as those with low κ [16]. Similar κ values have been reported in other literature for amorphous and crystalline IGZO, ranging from 1.0-1.4 W/mK [17-19]. The low κ of amorphous IGZO is said to be likely due to strong scattering vibration modes due to the structural randomness, while that of crystalline IGZO is probably caused by the perfect superlattice structure, inducing regular changes in acoustic impedances [16]. However, although the effect of crystallinity has been discussed in relation to κ, there are currently no literature comparing the amorphous and crystalline IGZO thin films from the viewpoint of the thermoelectric PF. Determining how to control the PF of IGZO of differing crystalline properties would provide a higher impact as it affects two of the three important thermoelectric properties. Moreover, electrical conductivity improvement via post-

deposition treatments, such as hydrogen annealing, plasma treatment or passivation, has been well reported for both amorphous and c-axis aligned crystalline IGZO, but their effects on the Seebeck coefficient has been left unexplored. Optimizing the post-deposition treatments can possibly enable easy functionality switching of IGZO from thin film transistor or memory device to thermoelectric generator, which can lead to the realization of future all-IGZO systems-on-panel.

A special type of c-axis aligned crystalline IGZO was developed by Yamazaki et. al in 2009 [20–28]. This material became an attractive alternative to both amorphous and single crystalline IGZO for thin film transistor applications owing to its relatively lower processing temperature but high reliability and low off-state leakage current [20-28]. Its unique structure cannot be classified as single crystalline, polycrystalline or nanocrystalline. Good crystallinity is observed along the c-axis, but individual crystals connected with hexagonal lattice distortions compose the a-b plane. The structure therefore possesses continuous crystal morphology without visible grain boundaries [20]. However, its thermoelectric properties have not been reported up to now.

In this work, the thermoelectric properties of commercial grade amorphous (a-IGZO), c-axis aligned crystalline (c-IGZO) and crystal-embedded c-axis aligned crystalline IGZO (cc-IGZO) are reported. This study also confirms which annealing conditions favor the highest thermoelectric power factor depending on the crystallinity. Specifically, the role of hydrogen incorporation on the crystal structure in relation to their thermal transport is discussed. Although electrical conductivity improvement via hydrogen on both amorphous and crystalline IGZO has already been reported elsewhere, its role on the Seebeck coefficient as well as the overall thermoelectric performance and stability has not yet been established.

2. Experimental methods

2.1 Sample Description

Three types of IGZO thin films deposited by RF sputtering on glass substrates were used in this study – amorphous (a-IGZO), c-axis aligned crystalline (c-IGZO) and crystal-embedded c-axis aligned crystalline (cc-IGZO). All samples were provided by Sharp Corporation [27-28]. The thickness of each sample was 200 nm. The c-IGZO sample is composed almost purely of c-axis aligned crystalline IGZO throughout the film, while the cc-IGZO is likewise mainly c-axis aligned crystalline but is embedded with crystals oriented differently. The a-IGZO, on the other hand, is uniformly amorphous. The samples were 75 cm × 62 cm in size, highly transparent and with initial sheet resistances of 0.15 MΩ/sq, 0.62 MΩ/sq and 11.1

TΩ/sq, respectively.

2.2 Characterization

To characterize the material and thermoelectric properties, samples having dimensions of 2 cm × 0.5 cm were cut from the panel-sized samples. Four electrodes were deposited via electron beam evaporation of Mo (50 nm) and Au (50 nm) thin films strips following a typical four-point probe configuration (Inset in Fig. 1b). Annealing was then performed at 673 K for 2 h to improve the thermoelectric properties using two different annealing environments, namely pure N_2 and N_2 with 4% H_2. To further understand the effect of hydrogen on the thermoelectric transport, 2% H_2-annealed samples were also made. X-ray diffraction was performed using Rigaku X-ray diffractometer (RINT-TTR III) from 2θ = 25−35º under Cu Kα radiation. Secondary ion mass spectroscopy (SIMS, ULVAC-PHI, Inc. ADEPT-1010) was then conducted using Cs^+ ion source (1 keV, 100 nA) to observe the relative amounts of oxygen and hydrogen on the samples. X-ray Photoelectron Spectroscopy (XPS, PHI5000 VersaProbeII, ULVAC-PHI) spectra were also measured at room temperature with Al-Kα radiation (1486.6 eV) to analyze the surface chemistry of the samples. Charging effects on the binding energies were calibrated with respect to the C 1s peak (284.8 eV). Transmission electron microscopy (TEM) image was obtained from JEOL JEM-3100FEF with operating voltage of 300 kV. Thermoelectric measurements were then performed using a physical properties measurement system (PPMS, Quantum Design EverCool II) from 100 to 400 K under vacuum conditions.

3. Results and discussion

The TEM images of the unannealed c-IGZO and cc-IGZO samples are shown in Fig. 1a and 1b, respectively. C-axis aligned crystals are arranged in columnar structures as seen in Fig. 1a, with the columns connected along the a-b plane via lattice distortions instead of actual grain boundaries. As previously discussed by the Yamazaki group, continuous crystallinity is maintained along the a-b plane owing to these lattice distortions, but does not impede charge transport as in the case of grain boundaries [20]. On the other hand, the cc-IGZO sample shows mainly c-axis oriented columnar crystals, but the presence of crystals revealing a different orientation can also be observed (boxed in Fig. 1b). Such crystal structures likely arose from some remaining amorphous portions in the film which crystallized at a later stage in the crystallization phase compared to its neighboring crystals.

The structural properties of the unannealed samples were also examined using X-ray diffraction (XRD). Figure 1c shows the normalized out-of-plane XRD spectra of the unannealed a-IGZO, c-IGZO and cc-IGZO samples. The a-IGZO samples simply revealed a broad amorphous IGZO peak at around 33º, and a wide 24º peak attributable to the silica glass substrate [18]. The c-IGZO and cc-IGZO samples, on the other hand, revealed a crystalline peak at about 2θ = 31º, which represents the (009) IGZO plane [20, 22-26]. This signifies the presence of c-axis aligned crystalline IGZO.

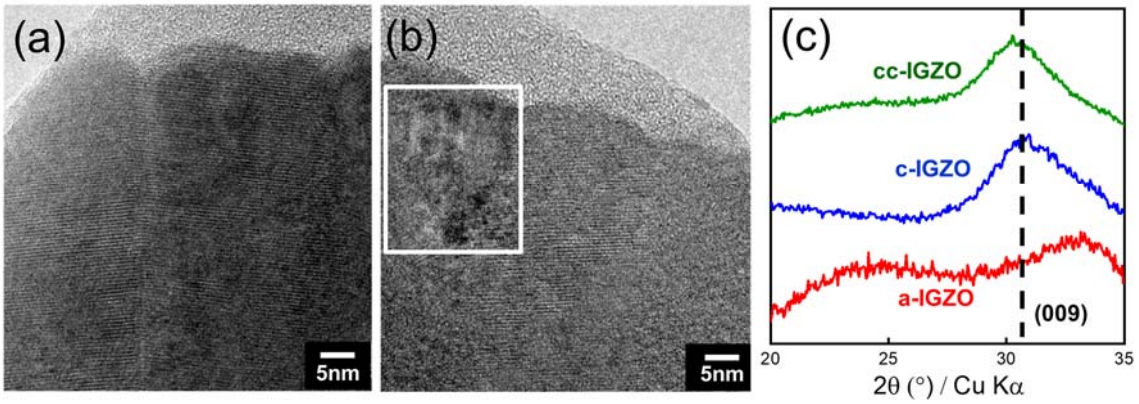

Fig. 1. TEM images of (a) c-IGZO and (b) cc-IGZO samples. (c) XRD spectra showing the (009) peak all unannealed IGZO thin film samples.

The thermoelectric performance of the annealed samples were then evaluated from 100 to 400 K and the properties are shown in Fig. 2. The N_2-annealed samples are referred to as a-N_2, c-N_2, and cc-N_2, while the samples annealed under N_2 with 4% H_2 are named a-H_2, c-H_2 and cc-H_2. The properties of the unannealed (UA) samples were not included as they exhibited resistance values way above the measurement system limit (< 2 MΩ). The electrical conductivities of all the samples in Fig. 1a displayed little temperature dependence, except for the cc-N_2 sample. The samples with the highest σ are the a-H_2 and the c-H_2 samples, with values of 463 S/cm and 327 S/cm at 100 K, respectively. Their N_2-annealed counterparts displayed lower electrical conductivities, suggesting that hydrogen incorporation is effective in increasing σ regardless of crystallinity, consistent with previous reports [20, 29–31]. The c-IGZO samples showed a similar trend, but remained at low σ values. The Seebeck coefficients, on the other hand, showed obvious temperature dependence. Also, an exact inverse trend with σ is observed for the a-IGZO and c-IGZO, wherein a-H_2 and c-N_2, which displayed the highest and the lowest σ, showed the lowest and

the highest S. This is expected since the carrier concentration, which is known to be directly proportional to σ, has an inverse effect on S. Finally, the PF of the samples showed a similar temperature dependence as with S. As shown in Fig. 1c, the highest PF value achieved is for the a-N_2 sample at 390 K, which is 0.093 mW/mK^2. For the crystalline samples, the highest PF is that of c-H_2, with 0.081 mW/mK^2, and 0.031 mW/mK^2 for cc-H_2 at 390 K.

To aid in understanding the effect of temperature on the electronic properties of the samples, a percolation conduction model is applied, as it has sufficiently explained the conduction behavior in previous ZnO-based thin films [32-33]. This conduction model suggests that the long-range electrical conduction is inhibited by energy barriers caused by structural randomness, which likely originates from the random distribution of Ga^{3+} and Zn^{2+} ions in the IGZO lattice. The temperature dependence of the percolation model states that the log σ generally shows a linear behavior with $T^{-1/4}$ following the equation: $\log \sigma = A - BT^{-1/4}$, where 1/B corresponds to the correlation radius of the conducting networks [32]. Shown in Fig. 1d is the graph of log σ vs $T^{-1/4}$ for all samples. Samples a-N_2 and c-H_2 showed a very weak decrease in log σ as $T^{-1/4}$ decreases. This suggests an almost metallic behavior, and such a decrease in σ as a function of T is likely induced by slight phonon scattering. On the other hand, the rest of the samples showed a direct linear proportionality with T, with the cc-N_2 exhibiting the largest slope. This perfectly resembles the thermal dependence behavior of the percolation conduction model. A higher negative slope indicates a greater tendency for thermal excitation to increase the number of electrons. This could probably explain the highest Seebeck coefficients observed for the cc-N_2 sample at any temperature, followed by c-N_2 and a-N_2.

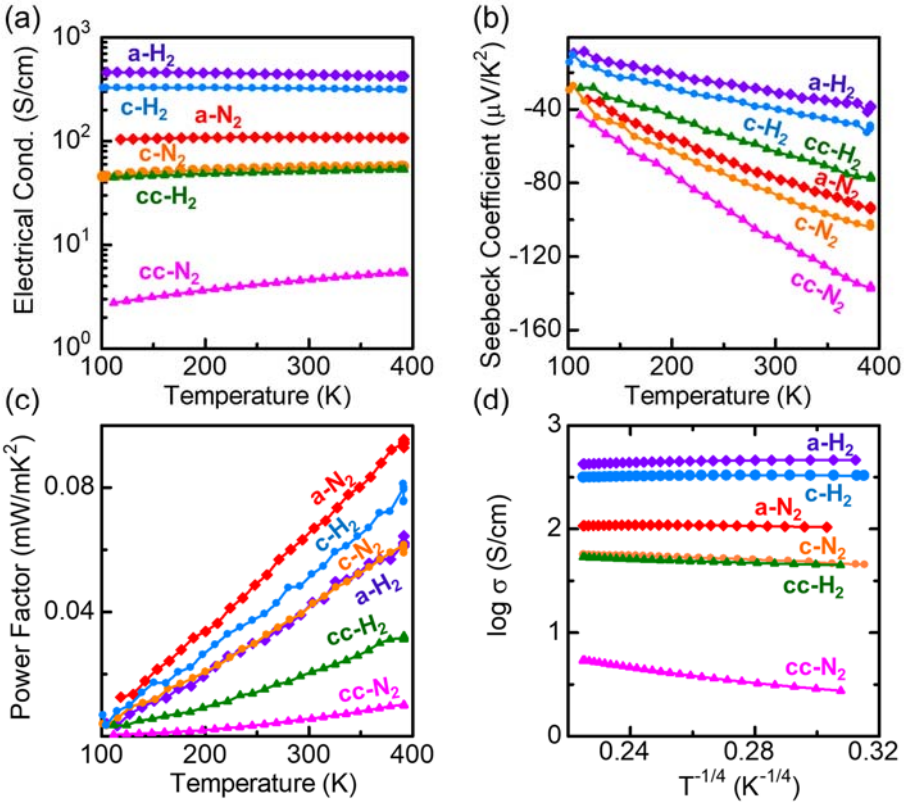

Fig. 2. (a) Electrical conductivity, (b) Seebeck coefficient and (c) power factor values of all IGZO samples from 100 to 400 K, and (d) plot of log σ vs $T^{-1/4}$.

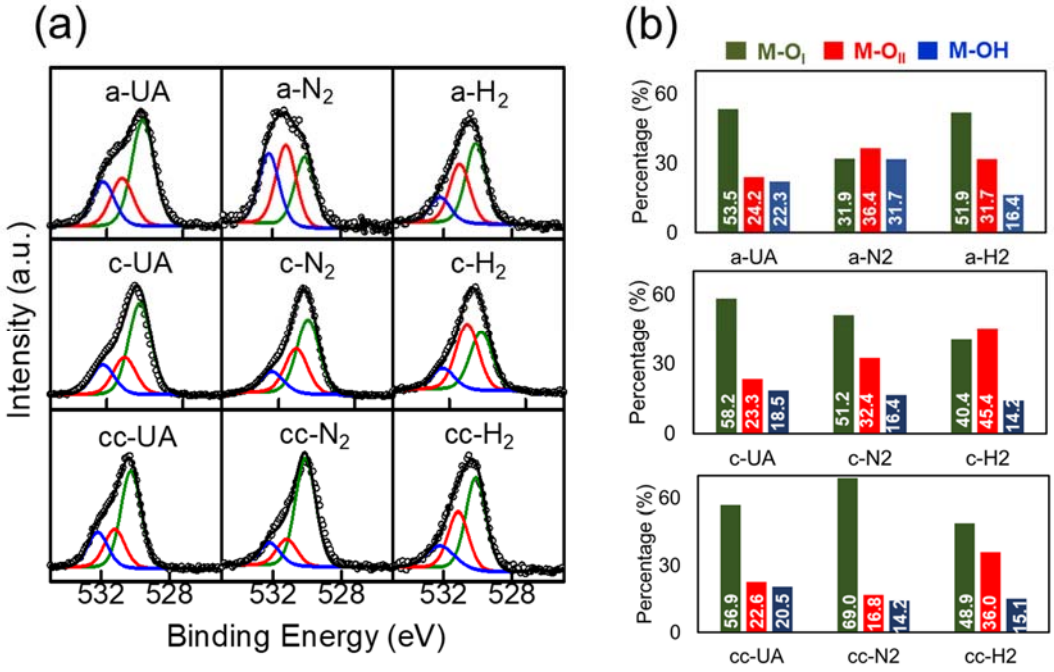

Fig. 3. (a) High-resolution XPS O1s peaks of the unannealed (UA), pure N_2-annealed and N_2 with 4% H_2-annealed samples, and (b) the corresponding peak area percentages of the O1s deconvoluted peaks.

In order to provide a deeper insight regarding the oxygen-related defects, which usually plays a major role in the electrical properties of IGZO, the O1s core level XPS spectra of all the samples were investigated and displayed in Fig. 3. The O1s can be deconvoluted into three peaks located at 530.2 ± 0.1 eV, 531.1 ± 0.1 eV and 532.4 ± 0.2 eV, which can typically be attributed to oxygen in metal oxide lattice (M-O_I), oxygen in the IGZO lattice with oxygen vacancies (M-O_{II}), and hydroxyl and other carbon-related impurities (M-OH), respectively [34]. The relative percentages of the deconvoluted peaks in each sample are quantified in Fig. 3b. Among the unannealed samples, the a-IGZO sample revealed the least amount of M-O and the highest amount of M-O_{II}. This is likely due to the highly ordered structure of both the crystalline samples, wherein M-O bonds are more intact. In contrast, M-O_{II} formation is most likely to occur in a-IGZO owing to the short-range order. Annealing with N_2 revealed varying effects depending on the crystallinity. In a-IGZO, the M-O_{II} greatly increased as expected, since the Vo formation is enhanced by heating paired with exposure to an O_2-poor environment. A similar effect was observed on c-IGZO, although the M-O maintained its dominance over the M-O_{II}. However, for the cc-IGZO sample, annealing with pure N_2 did not increase the M-O_{II}. Instead, it greatly enhanced the M-O bonds. This suggests that the structure is highly stable, such that oxygen-related defects are very difficult to form, as has been previously reported [35]. Introducing H_2 in the annealing environment also affected the samples differently. The c-H_2 revealed a great increase in M-O_{II} compared to the unannealed c-IGZO, which is in fact the highest of all the samples. A similar effect was observed with cc-H_2, although the M-O_{II} area percentage remained at a lower level. This suggests that the incorporation of H_2 in the annealing atmosphere for crystalline IGZO results to a concurrent increase in oxygen vacancies, as has been previously observed in CAAC-IGZO fabricated by the Yamazaki group [20]. However, the lower amount of M-O_{II} in a-H_2 compared to a-N_2 suggests that the H atoms could have been simultaneously passivating some of the Vo as they form. This can also explain the lower amount of M-OH in the H_2-annealed samples compared to the N_2-annealed samples for the a-IGZO and c-IGZO, since the H^+ could have been bonding with the metallic dangling bonds or existing as interstitial defects. It should be noted, however, that the trend exhibited by the samples in terms of amount of M-O_{II} does not exactly coincide with that of σ. For example, the a-H_2 sample exhibited the highest σ, but possessed one of the lowest amounts of M-O_{II}. This greatly implies that the Vo is not the only key player in enhancing the σ and the PF. As H^+ is a well-known source of free carriers whether as a substitutional or interstitial defect, it is probably equally responsible for the thermoelectric behavior of the samples.

To prove this, the effect of hydrogen on the samples was further investigated by varying the H_2 concentration in the N_2 annealing atmosphere (0%, 2% and 4%). Displayed in Fig. 4 is the effect of hydrogen concentration on the PF, σ and S of the samples at 300 K. The PF of the samples obviously exhibited varying reactions to increasing amount of hydrogen – the a-IGZO being negatively affected, the c-IGZO only slightly changing, and the cc-IGZO greatly increasing. The σ of c-IGZO and cc-IGZO appeared to be increasing with the amount of hydrogen, while the a-IGZO seemed to have peaked at 2%. The positive effect on both the σ and PF of the c-IGZO and cc-IGZO samples supports the previous observation that H is effective in improving the electrical properties. In the case of a-H_2, it is likely that there is only an optimum amount of hydrogen that aids in its electron transport, and an excess amount possibly introduces a large amount of interstitial defects [31]. The S displayed a perfectly inverse effect as with σ. Both c-IGZO and cc-IGZO samples exhibited decreasing S with % hydrogen, while a-IGZO displayed the lowest S at 2%. This can be related to their electron mobility values. This is known to be inversely proportional with effective mass, which in turn directly relates with S [36]. Introducing hydrogen into the system passivates the defects, leading to reduced trap sites and improved electron mobility. This decreases the effective mass, which translates to lower S values.

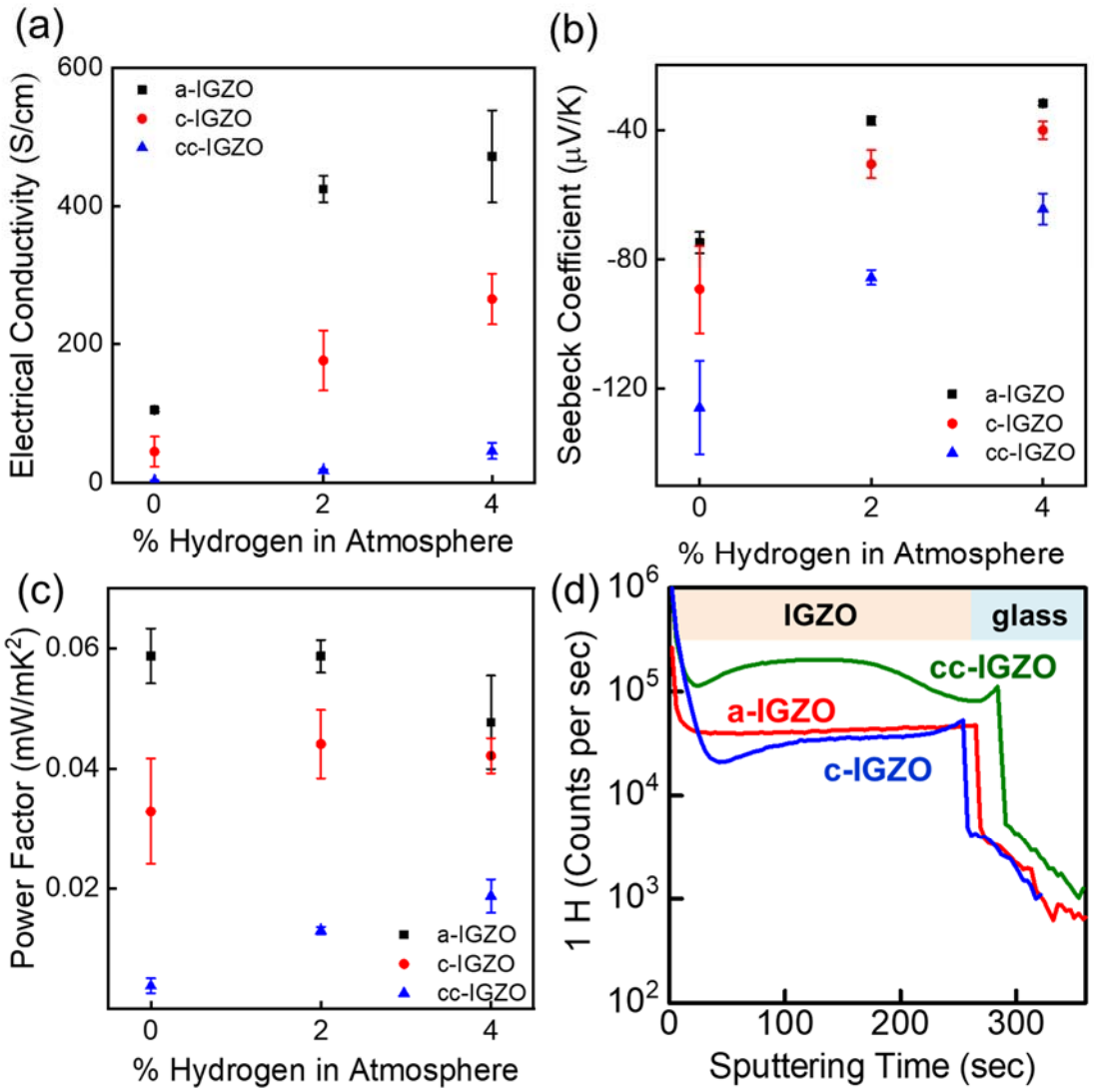

Fig. 4. (a) Power factor, (b) electrical conductivity and (c) Seebeck coefficient values of IGZO samples as an effect of increasing % hydrogen in the N_2 annealing atmosphere. (d) SIMS 1H spectrum of all H_2-annealed IGZO samples.

It is also important to determine how much of the hydrogen in the annealing environment is being incorporated in the samples, and if it depends on their crystallinity. SIMS analysis was then employed to look into the differences in hydrogen content of the hydrogen-annealed samples. The normalized SIMS spectra are presented in Fig. 4d. The amount of hydrogen is the highest with cc-IGZO, followed by the a-IGZO, and then the c-IGZO. It can also be observed that the amount of hydrogen is constantly varying with increasing penetration depths for both cc-IGZO and c-IGZO samples, as opposed to the a-IGZO sample

which exhibited an almost uniform amount of hydrogen all throughout the thin film depth. The high H amounts in the cc-IGZO film possibly provide an explanation on the great effect on its TE properties as an effect of % H_2. Increasing the hydrogen content could probably further improve the properties of cc-IGZO, but is not very safe especially for large scale fabrication processes. In the case of c-IGZO and a-IGZO, although their H contents are about the same level, a-H_2 still possesses much greater σ than c-H_2. This implies that the combined effect of Vo and H is important in maximizing the thermoelectric PF, and that the mechanisms are different depending on the crystallinity.

A Jonker plot was also constructed and shown in Fig. 5a to provide an insight on the degeneracy of the IGZO depending on crystallinity as an effect of the % H_2. Jonker plots revealed slopes of 70.9, 60.0 and 54.3 μV/K for the a-IGZO, c-IGZO and cc-IGZO samples, respectively. Positive values indicate typical n-type characteristic. In nondegenerate semiconductors, the relationship between S and log σ can be expressed by $S = \pm k/e(\ln\sigma - \ln\sigma 0)$ [14]. Therefore, the Jonker slope of a typical nondegenerate semiconductor is a constant value, which is about 198 μV/K [14]. Since the slopes of all samples did not coincide with this value, the samples then do not tend to behave like a typical non-degenerated semiconductor. This could be related to the metallic behavior exhibited by the H_2-annealed samples as explained above. This suggests that the incorporation of hydrogen in the annealing atmosphere may lead to a degenerated behavior for the InGaZnO, which translates to extremely high electrical conductivities, but not necessarily high PF.

To more clearly illustrate the effect of hydrogen on the PF, the measured PF of all samples were plotted against σ in Fig. 5b. The UA sample for cc-IGZO was excluded due to its extremely high resistance. A theoretical plot of the relationship between σ and PF was also included, which was calculated using the Kamiya-Nomura percolation model in IGZO [14, 37–38]. Standard Boltzmann transport formalism is applied using the percolation conduction model earlier described. The calculation is based on the mathematical approach proposed by Adler, et. al. [39]. The measured properties of the samples fit quite well with the theoretical PF values, which suggests that a-IGZO achieved nearly the maximum PF. This could be due to high Vo formation at pure N_2 annealing. It has been previously reported that Vo acts as a deep donor, which is likely why the free carriers generated only led to a moderately desirable σ value [40-41]. Combined with the moderate S values of a-IGZO, which probably originated from the high effective mass due to the high density of defects that traps the electrons, an almost maximum PF is achieved. The c-IGZO, however, could probably reach a higher PF when the conductivity can be controlled to range from 100–280

S/cm. Vo formation could be more difficult in the case of c-IGZO compared to a-IGZO due to the more orderly structure, which is likely why additional free carriers from hydrogen-related defects such as hydrogen substitution onto Vo sites (Ho) or interstitial H^+ are needed to achieve the optimum σ values. Both Ho and interstitial H^+, in contrast with the deep donor Vo, are said to act as shallow donor-like states and therefore greatly contribute to improved electron conduction in c-IGZO [40-41]. Also, the unique c-axis aligned crystallinity paired with the superlattice structure likely improves the interfacial phonon scattering, leading to higher S compared to a-H_2. Finally, cc-IGZO shows potential to reach maximum PF when σ can be further enhanced, but as earlier mentioned, increasing the hydrogen amount in the annealing environment is not very practical. The embedded crystals in the cc-IGZO thin film could be hindering the electron transport, which is likely the cause for the extremely high initial resistance. However, they contributed greatly to increasing the S, wherein the cc-N_2 achieved the highest S among all the samples. Therefore, in the case of a-IGZO, the best condition to maximize the thermoelectric PF is by the Vo-driven pure N_2 annealing, while for c-IGZO and cc-IGZO, the Ho-driven H_2 annealing is ideal.

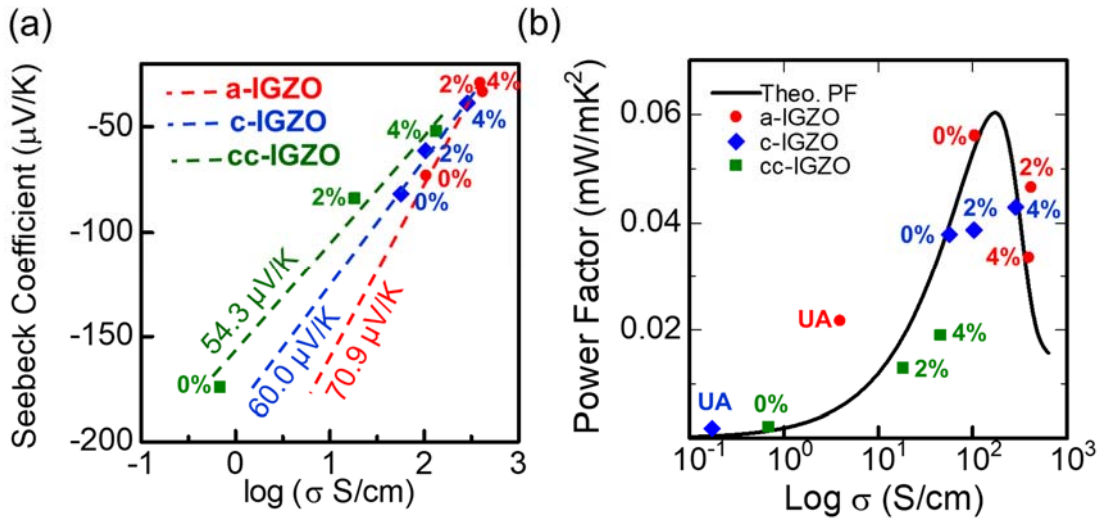

Fig. 5. (a) Jonker plot as an effect of % H_2, and (b) Log σ-PF plot of all IGZO samples plotted against theoretical PF.

4. Conclusions

The thermoelectric properties of amorphous, c-axis aligned crystalline and crystal-embedded c-axis aligned crystalline IGZO were reported in this study. Varying the annealing atmosphere by incorporating hydrogen was also performed to determine the ideal annealing environment depending on the crystalline type, and investigate which driving forces are responsible in enhancing their thermoelectric power factor. The a-N_2 and c-H_2 samples displayed the highest thermoelectric performances, while the cc-IGZO retained relatively low power factors even after annealing. XRD analysis revealed that H_2 annealing successfully retained the c-axis alignment for both the c-IGZO and cc-IGZO samples, which was likely responsible for obtaining better properties. The oxygen-related defects as well as the hydrogen contents of the samples were also investigated using XPS and SIMS, respectively, which revealed that for a-IGZO, the formation of a high amount of Vo is responsible for its superior thermoelectric properties, while the combined effect of Vo and Ho is the driving force in the case of both c-IGZO and cc-IGZO.

Acknowledgments

The authors gratefully acknowledge the Sharp Corporation for providing the InGaZnO samples.

References

1) K. Nomura, H. Ohta, A. Takagi, T. Kamiya, M. Hirano, and H. Hosono, Nature **432**, 488–492 (2004).
2) C. Kulchaisit, J. P. S. Bermundo, M. N. Fujii, Y. Ishikawa, and Y. Uraoka, AIP Adv. **8**, 095001 (2018).
3) S. J. Kim, S. Yoon, and H. J. Kim, Jpn. J. Appl. Phys. **53**, 02BA02 (2014).
4) P. Heremans, A. K. Tripathi, A.de Jamblinne de Meux, E. C. P. Smits, B. Hou, G. Pourtois, and G. H. Gelinck, Adv. Mater. **28**, 4266–4282 (2016).
5) S. Jeong, J. Lee, S. S. Lee, Y. Seo, S. Kim, J. Park, B. Ryu, W. Yang, J. Moon, and Y. Choi, J. Mater. Chem. C **1**, 4236–4243 (2013).
6) J. C. Felizco, M. Uenuma, D. Senaha, Y. Ishikawa, and Y. Uraoka, Appl. Phys. Lett. **111**, 033104 (2017).
7) J. C. Felizco, M. Uenuma, D. Senaha, Y. Ishikawa, and Y. Uraoka, IEEE 24th International Workshop on Active-Matrix Flatpanel Displays and Devices (AM-FPD), 283–284 (2017).
8) K. Umeda, M. Uenuma, D. Senaha, J. C. Felizco, Y. Uraoka, and H. Adachi, J. Phys. Conf.

Ser. **1052**, 012016 (2018).

9) Y. Yamauchi, Y. Kamakura, Y. Isagi, T. Matsuoka, and S. Malotaux, Jpn. J. Appl. Phys. **53**, 089201 (2014).
10) T. Hwang, I. Yang, O. Kwon, M. Ryu, C. Byun, C. Hwang, and S. K. Park, Jpn. J. Appl. Phys. **50**, 03CB06 (2011).
11) K. Kado, M. Uenuma, K. Sharma, H. Yamazaki, S. Urakawa, Y. Ishikawa, and Y. Uraoka, Appl. Phys. Lett. **105**, 123506 (2014).
12) C. Hsu, Y. Fan, and P. Liu, Appl. Phys. Lett. **102**, 062905 (2013).
13) J. Hou, S. Chang, C. Wu, H. Hong, and T. Hsueh, ECS J. Solid State Sci. Technol. **6**, Q120–Q122 (2017).
14) Y. Fujimoto, M. Uenuma, Y. Ishikawa, and Y. Uraoka, AIP Adv. **5**, 097209 (2015).
15) M. Uenuma, K. Umeda, J. Felizco, D. Senaha, and Y. Uraoka, J. Elec. Mater. **48**, 1971–1975 (2019).
16) B. Cui, L. Zeng, D. Keane, M. Bedzyk, D. Buchholz, R. Chang, X. Yu, J. Smith, T. Marks, Y. Xia, A. Facchetti, J. Medvedeva and M. Grayson, J. Phys. Chem. C **120**, 7467−7475 (2016).
17) M. Uenuma, J. C. Felizco, D. Senaha and Y. Uraoka, IOP Conf. Series: Journal of Physics: Conf. Series **1052**, 012011 (2018).
18) T. Yoshikawa, T. Yagi, N. Oka, J. Jia, Y. Yamashita, K. Hattori, Y. Seino, N. Taketoshi, T. Baba, and Y. Shigesato, Appl. Phys. Express, **6**, 021101 (2013).
19) D. Seo, S. Shin, H. Cho, B. Kong, D. Whang, and H. Cho, Acta Mater. **59**, 17, 6743-6750 (2011).
20) N. Kimizuka and S. Yamazaki, *Physics and Technology of Crystalline Oxide Semiconductor CAAC-IGZO: Fundamentals* (John Wiley & Sons, Ltd., Chichester, 2016) 2nd ed.
21) M. Lee and J. Dho, J. Kor. Phys. Soc. **58**, 3, pp. 492∼497 (2011).
22) S. Yamazaki, S. Ohshita, M. Oota, H. Baba, T. Onuki, H. Kunitake, K. Ohshima, D. Shimada, H. Kimura, T. Murakawa, T. Atsumi, and K. Kato, Int. J. Ceramic Eng. Sci. **1**, 6–20 (2019).
23) S. Yamazaki, T. Atsumi, K. Dairiki, K. Okazaki and N. Kimizuka, ECS J. Solid State Sci. Technol. **3**, Q3012–Q3022 (2014).
24) S. Yamazaki, ECS Trans. **64**, 155–164 (2014).
25) S. Yamazaki, H. Suzawa, K. Inoue, K. Kato, T. Hirohashi, K. Okazaki, and N. Kimizuka, Jpn. J. Appl. Phys. **53**, 04ED18 (2014).

26) M. Kozuma, Y. Okamoto, T. Nakagawa, T. Aoki, M. Ikeda, T. Osada, Y. Kurokawa, T. Ikeda, N. Yamade, Y. Okazaki, H. Miyairi, M. Fujita, J. Koyama, and S. Yamazaki, Jpn. J. Appl. Phys. **53**, 04EE12 (2014).
27) S. Yamazaki, J. Koyama, Y. Yamamoto, and K. Okamoto, SID 2012 Digest, 183−186 (2012).
28) Y. Yamada, D. Matsubayashi, S. Matsuda, Y. Sato, M. Ota, D. Ito, M. Tsubuku, Masahiro Takahashi, Takuya Hirohashi, Masayuki Sakakura, and Shunpei Yamazaki, Jap. J. Appl. Phys **53**, 091102 (2014).
29) H. Li, Y. Guo, and J. Robertson, Sci. Rep. 7, 16858 (2017).
30) A. Abliz, Q. Gao, D. Wan, X. Liu, L. Xu, C. Liu, C. Jiang, X. Li, H. Chen, T. Guo, J. Li and L. Liao, ACS Appl. Mater. Inter. **9**, 10798−10804 (2017).
31) Y. Nam, H. Kim, S. H. Cho, and S. K. Park, RSC Adv. **8**, 5622−5628 (2018).
32) H. Sim, S. Choi, J. Park, J. Song, S. Han, C. S. Hwang, and D. Cho, ECS J. Solid State Sci. Technol. **3**, P10–P12 (2014).
33) A. Takagi, K. Nomura, H. Ohta, H. Yanagi, T. Kamiya, M. Hirano and H. Hosono, Thin Solid Films **486**, 38–41 (2005).
34) J. C. C. Fan and J. B. Goodenough, J. Appl. Phys. **48**, 3524−3531 (1977).
35) T. Hiramatsu, M. Nakashima, E. Kikuchi, N. Ishihara, M. Tsubuku, K. Dairiki and S. Yamazaki, Jpn. J. Appl. Phys. **55**, 021203 (2016).
36) N. H. T. Nguyen, T. H. Nguyen, Y. Liu, M. Aminzare, A. T. T. Pham, S. Cho, D. P. Wong, K. Chen, T. Seetawan, N. K. Pham, H. K. T. Ta, V. C. Tran, and T. B. Phan, ACS Appl. Mater. Inter. **8**, 33916−33923 (2016).
37) T. Kamiya, K. Nomura, and H. Hosono, Appl. Phys. Lett. **96**, 122103 (2010).
38) T. Kamiya, K. Nomura, and H. Hosono, J. Display Technol. 5, 462–467 (2009).
39) D. Adler, L. Flora, and S. Senturia, Solid State Commun. 12, 9-12 (1973).
40) A. Janotti, and C. Van de Walle, Nature Materials 6, 44–47 (2007).
41) C. Chen, B. Yang, G. Li, H. Zhou, B. Huang, Q. Wu, R. Zhan, Y. Noh, T. Minari, S. Zhang, S. Deng, H. Sirringhaus, and C. Liu, Adv. Sci. 6, 1801189 (2019).